

MAGIC CONSTRAINTS ON  $\gamma$ -RAY EMISSION FROM CYGNUS X-3

- J. ALEKSIĆ<sup>1</sup>, L. A. ANTONELLI<sup>2</sup>, P. ANTORANZ<sup>3</sup>, M. BACKES<sup>4</sup>, C. BAIXERAS<sup>5</sup>, J. A. BARRIO<sup>6</sup>, D. BASTIERI<sup>7</sup>, J. BECERRA GONZÁLEZ<sup>8,9</sup>, W. BEDNAREK<sup>10</sup>, A. BERDYUGIN<sup>11</sup>, K. BERGER<sup>11</sup>, E. BERNARDINI<sup>12</sup>, A. BILAND<sup>13</sup>, O. BLANCH<sup>1</sup>, R. K. BOCK<sup>14</sup>, A. BOLLER<sup>13</sup>, G. BONNOLI<sup>2</sup>, P. BORDAS<sup>15</sup>, D. BORLA TRIDON<sup>14</sup>, V. BOSCH-RAMON<sup>15</sup>, D. BOSE<sup>6</sup>, I. BRAUN<sup>13</sup>, T. BRETZ<sup>16</sup>, D. BRITZGER<sup>14</sup>, M. CAMARA<sup>6</sup>, E. CARMONA<sup>14</sup>, A. CAROSI<sup>2</sup>, P. COLIN<sup>14</sup>, J. L. CONTRERAS<sup>6</sup>, J. CORTINA<sup>1</sup>, M. T. COSTADO<sup>8,9</sup>, S. COVINO<sup>2</sup>, F. DAZZI<sup>17,26</sup>, A. DE ANGELIS<sup>17</sup>, E. DE CEA DEL POZO<sup>18</sup>, B. DE LOTTO<sup>17</sup>, M. DE MARIA<sup>17</sup>, F. DE SABATA<sup>17</sup>, C. DELGADO MENDEZ<sup>8,27</sup>, M. DOERT<sup>4</sup>, A. DOMÍNGUEZ<sup>19</sup>, D. DOMINIS PRESTER<sup>20</sup>, D. DORNER<sup>13</sup>, M. DORO<sup>7</sup>, D. ELSAESSER<sup>16</sup>, M. ERRANDO<sup>1</sup>, D. FERENC<sup>20</sup>, M. V. FONSECA<sup>6</sup>, L. FONT<sup>5</sup>, R. J. GARCÍA LÓPEZ<sup>8,9</sup>, M. GARCZARCZYK<sup>8</sup>, M. GAUG<sup>8</sup>, N. GODINOVIC<sup>20</sup>, F. GÖEBEL<sup>14,28</sup>, D. HADASCH<sup>18</sup>, A. HERRERO<sup>8,9</sup>, D. HILDEBRAND<sup>13</sup>, D. HÖHNE-MÖNCH<sup>16</sup>, J. HOSE<sup>14</sup>, D. HRUPEC<sup>20</sup>, C. C. HSU<sup>14</sup>, T. JOGLER<sup>14</sup>, S. KLEPSE<sup>1</sup>, T. KRÄHENBÜHL<sup>13</sup>, D. KRANICH<sup>13</sup>, A. LA BARBERA<sup>2</sup>, A. LAILLE<sup>21</sup>, E. LEONARDO<sup>3</sup>, E. LINDFORS<sup>11</sup>, S. LOMBARDI<sup>7</sup>, F. LONGO<sup>17</sup>, M. LÓPEZ<sup>7</sup>, E. LORENZ<sup>13,14</sup>, P. MAJUMDAR<sup>12</sup>, G. MANEVA<sup>22</sup>, N. MANKUZHIIYIL<sup>17</sup>, K. MANNHEIM<sup>16</sup>, L. MARASCHI<sup>2</sup>, M. MARIOTTI<sup>7</sup>, M. MARTÍNEZ<sup>1</sup>, D. MAZIN<sup>1</sup>, M. MEUCCI<sup>3</sup>, J. M. MIRANDA<sup>3</sup>, R. MIRZOYAN<sup>14</sup>, H. MIYAMOTO<sup>14</sup>, J. MOLDÓN<sup>15</sup>, M. MOLES<sup>19</sup>, A. MORALEJO<sup>1</sup>, D. NIETO<sup>6</sup>, K. NILSSON<sup>11</sup>, J. NINKOVIC<sup>14</sup>, R. ORITO<sup>14</sup>, I. OYA<sup>6</sup>, S. PAIANO<sup>7</sup>, R. PAOLETTI<sup>3</sup>, J. M. PAREDES<sup>15</sup>, S. PARTINI<sup>3</sup>, M. PASANEN<sup>11</sup>, D. PASCOLI<sup>7</sup>, F. PAUSS<sup>13</sup>, R. G. PEGNA<sup>3</sup>, M. A. PEREZ-TORRES<sup>19</sup>, M. PERSIC<sup>17,23</sup>, L. PERUZZO<sup>7</sup>, F. PRADA<sup>19</sup>, E. PRANDINI<sup>7</sup>, N. PUCHADES<sup>1</sup>, I. PULJAK<sup>20</sup>, I. REICHARDT<sup>1</sup>, W. RHODE<sup>4</sup>, M. RIBÓ<sup>15</sup>, J. RICO<sup>24,1</sup>, M. RISSI<sup>13</sup>, S. RÜGAMER<sup>16</sup>, A. SAGGION<sup>7</sup>, K. SAITO<sup>14</sup>, T. Y. SAITO<sup>14,\*</sup>, M. SALVATI<sup>2</sup>, M. SÁNCHEZ-CONDE<sup>19</sup>, K. SATALECKA<sup>12</sup>, V. SCALZOTTO<sup>7</sup>, V. SCAPIN<sup>17</sup>, C. SCHULTZ<sup>7</sup>, T. SCHWEIZER<sup>14</sup>, M. SHAYDUK<sup>14</sup>, S. N. SHORE<sup>25</sup>, A. SIERPOWSKA-BARTOSIK<sup>10</sup>, A. SILLANPÄÄ<sup>11</sup>, J. SITAREK<sup>14,10</sup>, D. SOBCZYNSKA<sup>10</sup>, F. SPANIER<sup>16</sup>, S. SPIRO<sup>2</sup>, A. STAMERRA<sup>3</sup>, B. STEINKE<sup>14</sup>, J. C. STRUEBIG<sup>16</sup>, T. SURIC<sup>20</sup>, L. TAKALO<sup>11</sup>, F. TAVECCHIO<sup>2</sup>, P. TEMNIKOV<sup>22</sup>, T. TERZIC<sup>20</sup>, D. TESCARO<sup>1</sup>, M. TESHIMA<sup>14</sup>, D. F. TORRES<sup>24,18</sup>, H. VANKOV<sup>22</sup>, R. M. WAGNER<sup>14</sup>, Q. WEITZEL<sup>13</sup>, V. ZABALZA<sup>15</sup>, F. ZANDANEL<sup>19</sup>, R. ZANIN<sup>1,\*</sup> (THE MAGIC COLLABORATION)
- A. BULGARELLI<sup>29</sup>, W. MAX-MOERBECK<sup>30</sup>, G. PIANO<sup>31</sup>, G. POOLEY<sup>32</sup>, A. C. S. READHEAD<sup>30</sup>, J. L. RICHARDS<sup>30</sup>, S. SABATINI<sup>33</sup>, E. STRIANI<sup>31</sup>, M. TAVANI<sup>31,33</sup>, S. TRUSHKIN<sup>34</sup>
- <sup>1</sup> IFAE, Edifici Cn., Campus UAB, E-08193 Bellaterra, Spain  
<sup>2</sup> INAF National Institute for Astrophysics, I-00136 Rome, Italy  
<sup>3</sup> Università di Siena, and INFN Pisa, I-53100 Siena, Italy  
<sup>4</sup> Technische Universität Dortmund, D-44221 Dortmund, Germany  
<sup>5</sup> Universitat Autònoma de Barcelona, E-08193 Bellaterra, Spain  
<sup>6</sup> Universidad Complutense, E-28040 Madrid, Spain  
<sup>7</sup> Università di Padova and INFN, I-35131 Padova, Italy  
<sup>8</sup> Instituto de Astrofísica de Canarias, E-38200 La Laguna, Tenerife, Spain  
<sup>9</sup> Departamento de Astrofísica, Universidad, E-38206 La Laguna, Tenerife, Spain  
<sup>10</sup> University of Łódź, PL-90236 Lodz, Poland  
<sup>11</sup> Tuorla Observatory, University of Turku, FI-21500 Piikkiö, Finland  
<sup>12</sup> Deutsches Elektronen-Synchrotron (DESY), D-15738 Zeuthen, Germany  
<sup>13</sup> ETH Zurich, CH-8093 Switzerland  
<sup>14</sup> Max-Planck-Institut für Physik, D-80805 München, Germany  
<sup>15</sup> Universitat de Barcelona (ICC/IEEC), E-08028 Barcelona, Spain  
<sup>16</sup> Universität Würzburg, D-97074 Würzburg, Germany  
<sup>17</sup> Università di Udine, and INFN Trieste, I-33100 Udine, Italy  
<sup>18</sup> Institut de Ciències de l'Espai (IEEC-CSIC), E-08193 Bellaterra, Spain  
<sup>19</sup> Instituto de Astrofísica de Andalucía (CSIC), E-18080 Granada, Spain  
<sup>20</sup> Croatian MAGIC Consortium, Institute R. Boskovic, University of Rijeka and University of Split, HR-10000 Zagreb, Croatia  
<sup>21</sup> University of California, Davis, CA 95616-8677, USA  
<sup>22</sup> Institute for Nuclear Research and Nuclear Energy, BG-1784 Sofia, Bulgaria  
<sup>23</sup> INAF/Osservatorio Astronomico and INFN, I-34143 Trieste, Italy  
<sup>24</sup> ICREA, E-08010 Barcelona, Spain  
<sup>25</sup> Università di Pisa, and INFN Pisa, I-56126 Pisa, Italy  
<sup>26</sup> Supported by INFN Padova  
<sup>27</sup> Now at: Centro de Investigaciones Energéticas, Medioambientales y Tecnológicas (CIEMAT), Madrid, Spain  
<sup>28</sup> Deceased  
<sup>29</sup> INAF-IASF, Bologna, Italy  
<sup>30</sup> California Institute of Technology, Owens Valley Radio Observatory, Pasadena, CA 91125, USA  
<sup>31</sup> Università Tor Vergata, and INFN, I-00133 Rome, Italy  
<sup>32</sup> Cavendish Laboratory, Cambridge CB3 0HE, UK  
<sup>33</sup> INAF-IASF, I-00133 Rome, Italy  
<sup>34</sup> Special Astrophysical Observatory RAS, Nizhnij Arkhyz, Russia

\* corresponding authors. E-mail: roberta@ifae.es, tysaito@mpp.mpg.de

Accepted to ApJ 07/18/2010

## ABSTRACT

Cygnus X-3 is a microquasar consisting of an accreting compact object orbiting around a Wolf–Rayet star. It has been detected at radio frequencies and up to high-energy  $\gamma$  rays (above 100 MeV). However, many models also predict a very high energy (VHE) emission (above hundreds of GeV) when the source displays relativistic

persistent jets or transient ejections. Therefore, detecting such emission would improve the understanding of the jet physics. The imaging atmospheric Cherenkov telescope MAGIC observed Cygnus X-3 for about 70 hr between 2006 March and 2009 August in different X-ray/radio spectral states and also during a period of enhanced  $\gamma$ -ray emission. MAGIC found no evidence for a VHE signal from the direction of the microquasar. An upper limit to the integral flux for energies higher than 250 GeV has been set to  $2.2 \times 10^{-12}$  photons  $\text{cm}^{-2} \text{s}^{-1}$  (95% confidence level). This is the best limit so far to the VHE emission from this source. The non-detection of a VHE signal during the period of activity in the high-energy band sheds light on the location of the possible VHE radiation favoring the emission from the innermost region of the jets, where absorption is significant. The current and future generations of Cherenkov telescopes may detect a signal under precise spectral conditions.

*Subject headings:* acceleration of particles — binaries: general — gamma rays: general — methods: observational — X-rays: binaries

## 1. INTRODUCTION

Cygnus X-3 is a bright and persistent X-ray binary, discovered in 1966 (Giacconi *et al.* 1967), but the high-energy processes occurring in the source are still poorly understood. It lies close to the Galactic plane at a distance between 3.4 and 9.8 kpc, probably at 7 kpc, depending on different distance estimates to the Cygnus OB2 association (Ling *et al.* 2009). The nature and the mass of the compact object are still a subject for debate. Published results suggest either a neutron star of  $1.4 M_{\odot}$  (Stark & Saia 2003) or a black hole of less than  $10 M_{\odot}$  (Hanson *et al.* 2000). The identification of its donor star as a Wolf-Rayet star (van Kerkwijk *et al.* 1992) classifies it as a high-mass X-ray binary. Nevertheless Cygnus X-3 shows a short orbital period of 4.8 hr, typical of the low-mass binaries, which has been inferred from the modulation of both the X-ray (Parsignault *et al.* 1972) and infrared emissions (Becklin *et al.* 1973).

Despite the strong X-ray absorption in this system, which may be caused by the wind of the companion star, the X-ray spectrum has been intensively studied. The source shows two main spectral X-ray states resembling the canonical states of the black hole binaries: the hard state (HS) and the soft state (SS; Zdziarski & Gierlinski 2004; Hjalmarsson *et al.* 2008). The HS is characterized by a weak soft thermal component and a strong non-thermal power-law emission peaking at hard X-ray energies, whereas the SS, though showing a non-thermal tail (Szostek *et al.* 2008), is dominated by the optically thick thermal disk emission. In Cygnus X-3, however, the HS displays a high-energy cutoff at  $\approx 20$  keV, significantly lower than the  $\approx 100$  keV value found for black hole binaries (Hjalmarsson *et al.* 2004; Zdziarski & Gierlinski 2004).

Adding to its peculiarity, Cygnus X-3 is the brightest radio source among the X-ray binaries, quite frequently exhibiting huge radio flares (as intense as few thousand times the quiescent emission level of  $\sim 20$  mJy at 1.5 GHz; Braes & Miley 1972) first seen by Gregory *et al.* (1972). During these outbursts, which occur mainly when the source is in the SS, and last several days, Cygnus X-3 reveals the presence of collimated relativistic jets (e.g., Martí *et al.* 2001; Mioduszewski *et al.* 2001; Geldzahler *et al.* 1983; Miller-Jones *et al.* 2004). Thus, Cygnus X-3 has been classified as a microquasar. Based on arcsecond-scale radio observations and their relation with soft X-ray emission, six X-ray/radio states have been identified: quiescent (flux densities  $\sim 100$  mJy), minor flaring ( $< 1$  Jy), suppressed ( $< 100$  mJy), quenched ( $< 30$  mJy), major flaring ( $> 1$  Jy), and post-flaring (Szostek *et al.* 2008; Tudose *et al.* 2010; Koljonen *et al.* 2010). In the transition from the X-ray hard/radio quiescent state to the SS, the radio emission is

strongly suppressed, and if it reaches the quenched level, the source usually produces a major radio flare (Waltman *et al.* 1994).

Cygnus X-3 has also historically drawn a great deal of attention due to numerous claims of detection at TeV and PeV  $\gamma$  rays, using early-days detectors in these energy ranges (Vladimirsky *et al.* 1973; Danaher *et al.* 1981; Lamb *et al.* 1982; Dowthwaite 1983; Samorsky & Stamm 1983; Cawley *et al.* 1985; Chadwick *et al.* 1985; Bhat *et al.* 1986). However, a critical analysis of these observations raised doubts about their validity (Chardin & Gerbier 1989), and in recent years the more sensitive instruments have not confirmed those claims for energies above 500 GeV (Schilling *et al.* 2001; Albert *et al.* 2008a). Nevertheless, microquasars are believed to produce a very high energy (VHE) emission inside the jets: high density and magnetic fields provided by the accretion disk and by the companion star create favorable conditions for effective production of  $\gamma$  rays (Levinson & Blandford 1996; Romero *et al.* 2003; Bosch-Ramon *et al.* 2006). This radiation could have either an episodic nature due to the ejection of strong radio-emitting blobs (Atayan & Aharonian 1999), generally occurring in the SS in the case of Cygnus X-3 or a (quasi) stationary character being originated in the persistent compact jet present during the HS (Bosch-Ramon *et al.* 2006).

Using data from the Energetic Gamma-Ray Experiment Telescope detector aboard the Compton Gamma-Ray Observatory, Mori *et al.* (1997) reported an average flux of  $(8.2 \pm 0.9) \times 10^{-7}$  photons  $\text{cm}^{-2} \text{s}^{-1}$  at energies above 100 MeV coming from the direction of Cygnus X-3. However, no orbital modulation was detected in the signal, precluding a solid association. The experimental situation in the high-energy region has been drastically changed by the results recently published by *AGILE* (Tavani *et al.* 2009) and *Fermi*/LAT (Abdo *et al.* 2009). *AGILE* detected the source in five different moments, for a couple of days each, four of them corresponding to the peak emissions shown in the detailed *Fermi*/LAT light curve (see below). The last detection, occurred in 2009 July, has not been published yet by the *AGILE* Collaboration (A. Bulgarelli *et al.*, in preparation). On the other hand, *Fermi*/LAT detected a clear signal from Cygnus X-3 above 100 MeV during two periods of enhanced activity lasting for several weeks and coinciding with the source being in the SS. The measured flux is variable and shows an orbital modulation, which confirms the origin of the signal from the microquasar. The *AGILE* flux level is comparable with the one of the *Fermi*/LAT flux peaks, as high as  $2.0 \times 10^{-6}$  photons  $\text{cm}^{-2} \text{s}^{-1}$  above 100 MeV.

Observations of binary systems with imaging atmospheric Cherenkov telescopes (IACTs) in the VHE band have proven very fruitful in recent years, with the detection of the orbitally

modulated  $\gamma$ -ray emitters PSR B1259-63 (Aharonian et al. 2005a), LS 5039 (Aharonian et al. 2005b, 2006), and LS I +61 303 (Albert et al. 2006, 2008b, 2009; Acciari et al. 2008, 2009; Anderhub et al. 2009). However, these systems may be different from Cygnus X-3 since the radio and high-energy radiation could be produced in all three sources by the interaction of the winds of a star and an orbiting pulsar (Maraschi & Treves 1981; Tavani & Arons 1997; Dubus 2006). Nevertheless, Cygnus X-3 GeV  $\gamma$ -ray modulation presents some common features to those observed in LS 5039 and LS I +61 303. On the other hand, although observations of other well-established microquasars, such as GRS 1915+105 (Acero et al. 2009; Saito et al. 2009), did not reveal any signal, there is an interesting possibility of VHE emission from Cygnus X-1 (Albert et al. 2007a), still to be confirmed by an independent detection. The origin of this possible emission has been speculated to be linked to a maximum of the X-ray super-orbital modulation of the system (Rico 2008). Moreover, there is also a claim by *AGILE* about a Cygnus X-1 detection during a short flare (Sabatini et al. 2010, ATel 2512), which, however, has not been corroborated by *Fermi*/LAT yet<sup>1</sup>. Such experimental results endorsed by the theoretical predictions, have encouraged deeper observations of the black hole binaries in the VHE band.

This paper reports observations of Cygnus X-3 performed with the Major Atmospheric Gamma Imaging Cherenkov (MAGIC) telescope between 2006 and 2009. All these observations were carried out with the first stand-alone MAGIC telescope, MAGIC phase I. Cygnus X-3 observations were planned to cover different X-ray/radio states, including those that showed a strong high-energy  $\gamma$ -ray flux. This allowed us to search for VHE emission, above 250 GeV, from Cygnus X-3 in the different cases for which this radiation is predicted in theoretical scenarios. In addition, specific analyses were performed to look for predicted features, such as periodic and variable emission. Section 2 describes the performance of MAGIC and the observational strategy. The analysis chain is explained in Section 3. The results obtained by MAGIC in a multi-wavelength context are reported in Section 4. A brief discussion is given in Section 5.

## 2. OBSERVATIONS

MAGIC (phase I) is an IACT located at the Canary Island of La Palma (Spain), at  $28^{\circ}.8$  N–,  $17^{\circ}.8$  W, 2200 m above sea level. It is a 17 m diameter IACT with an energy threshold of 60 GeV (with the standard trigger). The collected Cherenkov light is focused on a multi-pixel camera composed of 576 photomultiplier tubes (PMTs).

The performance of the MAGIC telescope changed over the years. The largest improvement followed the upgrade of the 300 MHz readout system in 2007 February. The new multiplexed 2 GHz flash analog-digital converters improved the time resolution of the recorded shower images and reduced the contamination of the night sky background (Aliu et al. 2009). Accordingly, the telescope integral flux sensitivity improved from  $\approx 2.5\%$  to  $\approx 1.6\%$  of the Crab Nebula flux for energies greater than 270 GeV in 50 hr of observations. At these energies, the angular and energy resolutions are  $\approx 0^{\circ}.1$  and  $\approx 20\%$ , respectively. MAGIC can provide  $\gamma$ -ray point-like source localization in the sky with a precision of  $\approx 2'$  (Albert et al. 2008c). It is able to observe under moderate moonlight or twilight conditions (Albert et al. 2007b;

Britzger et al. 2009), which, causing an increase of the night sky background, can be monitored through the PMT anode direct currents (DCs).

MAGIC pointed toward Cygnus X-3 for a total of 69.2 hr between 2006 March and 2009 August. Since the source is expected to be variable, the observations were triggered by its state at other wavelengths. In 2006, observations were prompted by flares at radio frequencies. The MAGIC collaboration received two alerts from the RATAN-600 telescope on 2006 March 10 and on 2006 July 26 (S. Trushkin, private communication 2006). Both radio flares had an X-ray counterpart: the source was in the SS according to *RXTE*/ASM and *Swift*/BAT measurements. In 2007, the observations were triggered using public *RXTE*/ASM (1.5–12 keV) and *Swift*/BAT (15–50 keV) data, as follows: (1) *Swift*/BAT daily flux larger than  $0.05 \text{ counts cm}^{-2} \text{ s}^{-1}$  and (2) ratio between *RXTE*/ASM and *Swift*/BAT count rates lower than 200. These criteria guaranteed the source to be in the HS. During 2008 and 2009, MAGIC observed Cygnus X-3 following high-energy  $\gamma$ -ray alerts issued by the *AGILE* satellite. The first of these alerts arrived in 2008 April 18, the second one in 2009 July 18 (M. Tavani, private communication 2008; 2009). These last two campaigns occurred when the source was in the SS.

At La Palma, Cygnus X-3 culminates at a zenith angle of  $12^{\circ}$ . The observations were carried out at zenith angles between  $12^{\circ}$  and  $50^{\circ}$ . They were performed partially in a on-off mode and in a false-source tracking mode (wobble) (Fomin et al. 1994), the latter pointing to two directions at  $24'$  distance and opposite sides of the source. The entire Cygnus X-3 data set recorded by MAGIC amounts to 69.2 hr, out of which  $12.5 \text{ hr}^2$  were rejected from further analysis because of their anomalous event rates, leading to a total of 56.7 hr of useful data distributed in 39 nights of observation. The details of the observations are quoted in Table 1.

## 3. DATA ANALYSIS

Data analysis was carried out using the standard MAGIC calibration and analysis software: once the PMT signal pulses are calibrated (Albert et al. 2008d), pixels containing no useful information for the shower image reconstruction are discarded. This is done by an image cleaning procedure which takes into account the amplitude and the timing information of the calibrated signals (Aliu et al. 2009). The constraints on the signal amplitude are increased in the case of moonlight conditions, when the pixel DCs become larger than  $2.5 \mu\text{A}$  (see Table 1). This higher image cleaning allows us to use the standard Monte Carlo (MC) during the analysis of these data, without the need of any correction, as long as the average pixel DCs are below  $4 \mu\text{A}$  (Britzger et al. 2009).

Afterward, the surviving pixels are used to compute the Hillas event image parameters (Hillas 1985). In addition, Hillas and timing variables are combined into a single  $\gamma$ /hadron discriminator (*hadronness*) and an energy estimator by means of the Random Forest classification and regression algorithm, which takes into account the correlation between the different Hillas and timing variables (Breiman 2001; Albert et al. 2008e). These algorithms are trained with a sample of MC-simulated  $\gamma$ -ray events and a sample of back-

<sup>1</sup> Preliminary results can be found at <http://fermisky.blogspot.com/2010/03/lat-limit-on-cyg-x-1-during-reported.html>

<sup>2</sup> 9.6 hr were rejected due to high-altitude Saharan dust (calima), which affects the atmosphere above Canary islands and is more intense during sum-

TABLE 1  
CYGNUS X-3 OBSERVATION LOG<sup>a</sup>.

Obs. Cycle	Date (yyyy mm dd)	(MJD)	Eff. Time (h)	Zd (°)	DC <sup>b</sup> (μA)	Spectral State <sup>c</sup>
I	2006 03 23	53817	0.45	45–50	3.5	SS
	2006 03 24	53818	0.25	47–50	2.5	
	2006 03 26	53820	0.53	44–50	1.5	
	2006 03 28	53822	0.70	42–50	1.4	
	2006 03 30	53824	0.80	41–50	1.3	
	2006 03 31	53825	0.90	40–50	1.4	
	2006 04 01	53826	1.00	38–50	1.8	
	2006 04 02	53827	0.92	40–50	1.2	
II	2006 04 03	53828	1.05	38–50	1.2	SS
	2006 07 27	53943	3.10	12–34	1.2	
	2006 07 28	53944	2.53	12–31	1.1	
	2006 07 29	53945	1.73	12–20	1.2	
	2006 07 30	53946	1.36	12–20	1.1	
	2006 08 01	53948	0.92	12–20	1.4	
	2006 08 02	53949	1.88	12–19	1.2	
III	2007 07 06	54286	2.16	19–45	2.3	HS
	2007 07 07	54287	4.53	12–45	2.3	
	2007 07 08	54288	1.07	26–45	1.5	
	2007 07 09	54289	0.38	34–40	1.5	
	2007 07 14	54295	1.82	12–21	1.5	
	2007 07 15	54296	1.93	12–21	1.5	
	2007 07 16	54297	1.93	12–21	1.4	
	2007 07 24	54305	1.75	12–23	1.4	
	2007 07 26	54307	0.98	19–30	1.4	
	2007 07 27	54308	0.5	19–30	1.4	
	2007 08 04	54316	0.73	27–35	1.5	
	2007 08 06	54318	2.72	12–30	1.6	
	2007 08 07	54319	1.93	13–31	1.3	
	2007 08 08	54320	1.58	14–31	1.4	
	2007 09 03	54346	1.86	13–37	2.5	
IV	2008 04 28	54584	0.31	32–40	2.9	SS
	2008 04 29	54585	1.07	24–41	3.2	
	2008 04 30	54586	1.33	23–40	2.6	
V	2009 07 19	55031	3.48	12–36	1.2	SS
	2009 07 21	55033	2.21	14–42	1.2	
	2009 07 22	55034	1.63	12–27	1.1	
	2009 08 01	55044	1.81	17–39	1.5	
	2009 08 02	55045	0.88	27–41	1.6	

<sup>a</sup> From left to right: observational cycle, date of the beginning of the observations, also in MJD, effective time after quality cuts, zenith angle range, the anode PMT DCs, and the spectral state.

<sup>b</sup> The anode PMT DCs show the level of the moonlight conditions.

<sup>c</sup> Spectral state was derived by using *Swift*/BAT and *RXTE*/ASM data.

ground events extracted from real data. The used timing variables allow an improvement of the analysis sensitivity of a factor of 1.4 (1.2) in data recorded with the new ultra-fast (old 300 MHz) readout system (Aliu *et al.* 2009).

Images with a total charge below 200 photo-electrons were discarded from further analysis in order to homogenize the different data and MC samples and achieve a common stable energy threshold of all the analyses. The number of  $\gamma$ -ray candidates in the direction of the source is estimated by using the distribution of  $\alpha$  angle (Hillas 1985), which is related to the shower orientation. The evaluation of the background depends on the data taking mode. For data taken in the on-off mode in which the signal data sample is called “on” data, the background is estimated using a different sample, called “off” data. The latter has a similar amount of data recorded during the same epoch as the “on” sample at similar zenith angles and atmospheric conditions with no known  $\gamma$ -ray source in the field of view. For the observations carried out in the wobble mode, the background is extracted from three circular control regions, located symmetrically to the source position

with respect to the camera center.

The Cygnus X-3 data set extends over five different, one-year long cycles of observation, which are characterized by varying performances of the telescope. In addition, cycle I data were recorded in the on-off mode, all the others in the wobble mode, cycle IV data were taken under moderate moonlight conditions.

Each cycle of data was analyzed separately using the appropriate image cleaning procedure, and a matching sample of MC-simulated  $\gamma$ -ray events. The analysis selection cuts, on *hadronness* and *alpha*, for each cycle of data were obtained optimizing the sensitivity in a Crab Nebula sample and requiring at least 70%  $\gamma$ -ray selection efficiency. The selected Crab Nebula sample was recorded during the same cycle at similar zenith angles and in the same data taking mode.

All the analyses were then combined in order to calculate the integral flux upper limits (ULs) for energies greater than 250 GeV, which is the energy threshold of each cycle of data. The obtained ULs at the 95% confidence level (CL) were computed after Rolke *et al.* (2005) method assuming a Gaussian background and 30% of systematic uncertainties in the flux level (Albert *et al.* 2008c). The spectrum was assumed to be Crab like (Aharonian *et al.* 2004), with a photon index of 2.6. However, a 30% change in the photon index yields a variation of less than 1% in the ULs.

#### 4. RESULTS

A search for VHE  $\gamma$ -ray emission from Cygnus X-3 was performed separately for each cycle of observations. None of them yielded a significant excess. The combination of all the data samples yields a 95% CL upper limit to an integral flux of  $2.2 \times 10^{-12}$  photons  $\text{cm}^{-2} \text{s}^{-1}$  for energies greater than 250 GeV. It corresponds to 1.3% of the Crab Nebula flux at these energies. The differential flux ULs are shown in Table 2 and in Figure 1.

Given that Cygnus X-3 flux is variable at other energy bands on time scales of days,  $\gamma$ -ray signals were searched for also on a daily basis. No significant excess events were found in any observation night. The integral flux ULs for energies above 250 GeV are shown in Table 3 and in the top panel of Figure 2.

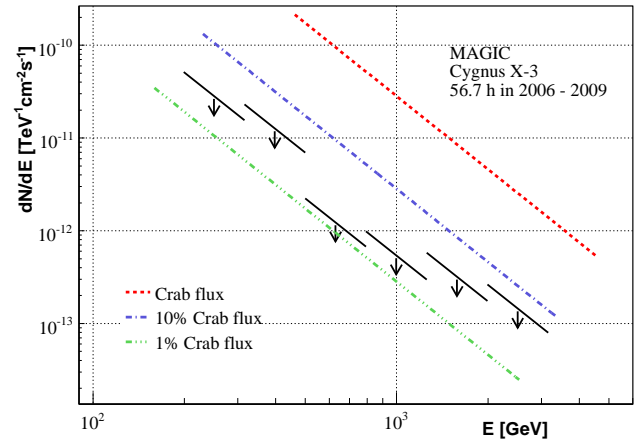


FIG. 1.— Differential flux ULs at 95% CL for the VHE time-integrated emission. The slope of the arrows indicates the assumed power-law spectrum with a photon index of 2.6.

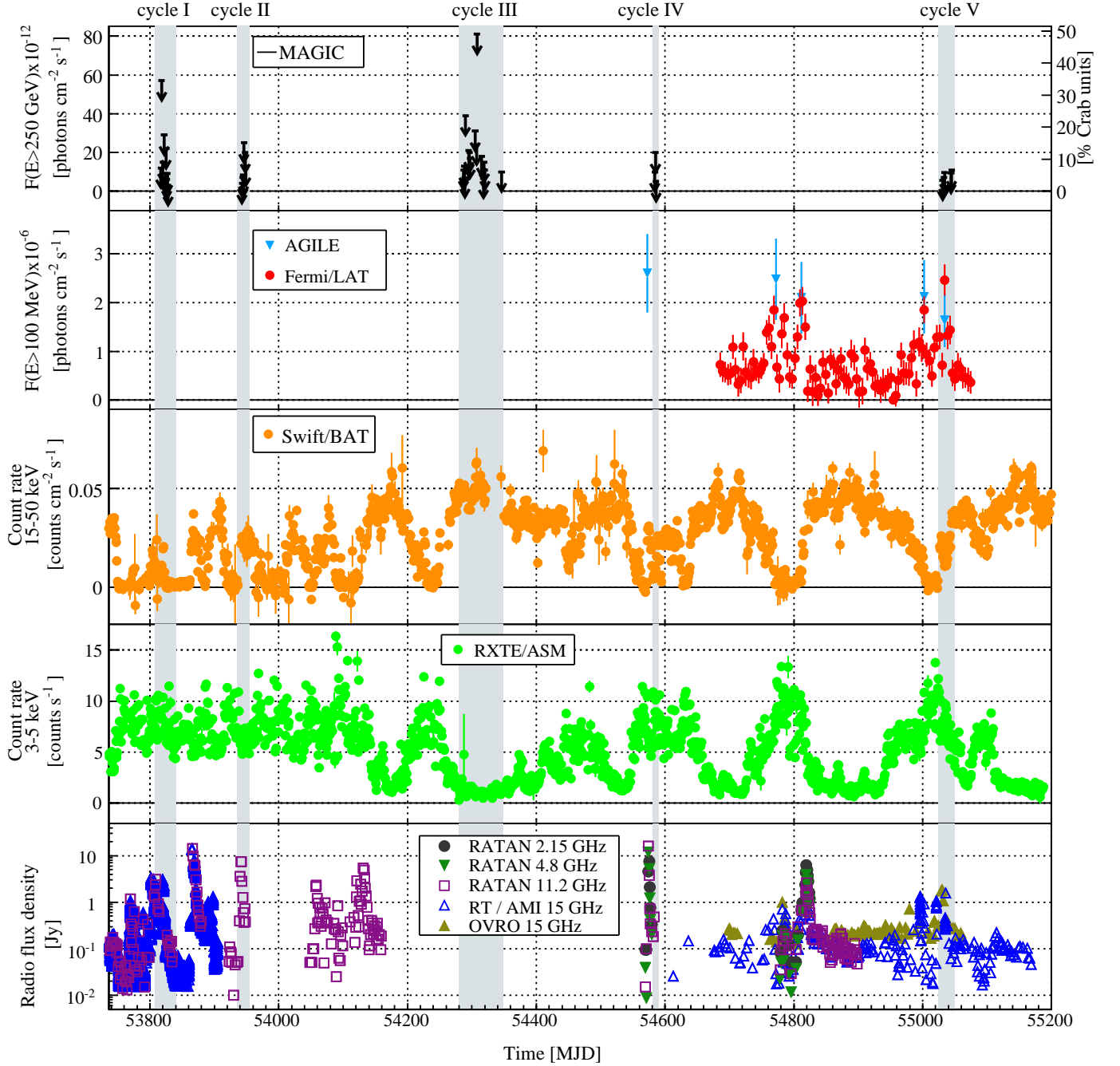


FIG. 2.— From top to bottom: daily MAGIC VHE integral flux ULs for  $E > 250$  GeV, high-energy  $\gamma$ -ray (*AGILE* and *Fermi/LAT*), hard X-ray (*Swift/BAT*), soft X-ray (*RXTE/ASM*), and radio fluxes measured for Cygnus X-3 as a function of time (from 2006 January 1 until 2009 December 15). The grey bands show the periods corresponding to the MAGIC observations. The OVRO and AMI 15 GHz data generally agree well, except for the offset apparent during steady periods which is due to unrelated extended emission resolved out by AMI.

In Figure 2, MAGIC results are presented in a multi-wavelength context where the above-mentioned flux variability at different energy bands is rather clear. In particular, it displays daily MAGIC VHE integral ULs, high-energy  $\gamma$ -ray (*AGILE* and *Fermi/LAT* (0.1–30 GeV)), hard X-ray (*Swift/BAT* (15–50 keV)), soft X-ray (*RXTE/ASM* (3–5 keV)), and radio measured fluxes from 2006 January 1 (MJD 53736) until 2009 December 15 (MJD 55180). The soft X-ray energy band of *RXTE/ASM* is between 1.5 and 12 keV, out of which only the 3–5 keV band was used, as it yields to

the cleanest radio/X-ray correlation (Szostek et al. 2008). The radio measurements, displayed in logarithmic scale, were provided by the RATAN-600 telescope at 2.15, 4.8, and 11.2 GHz and by the Ryle telescope (RT), the Arcminute Microkelvin Imager (AMI) telescope and the Owens Valley Radio Observatory (OVRO) 40 meter telescope at 15 GHz.

The soft and hard X-ray fluxes shown in Figure 2 allow us to derive the X-ray spectral state of Cygnus X-3 during MAGIC observations. Cycle III data are the only ones taken when the source was in the HS, as requested by the obser-

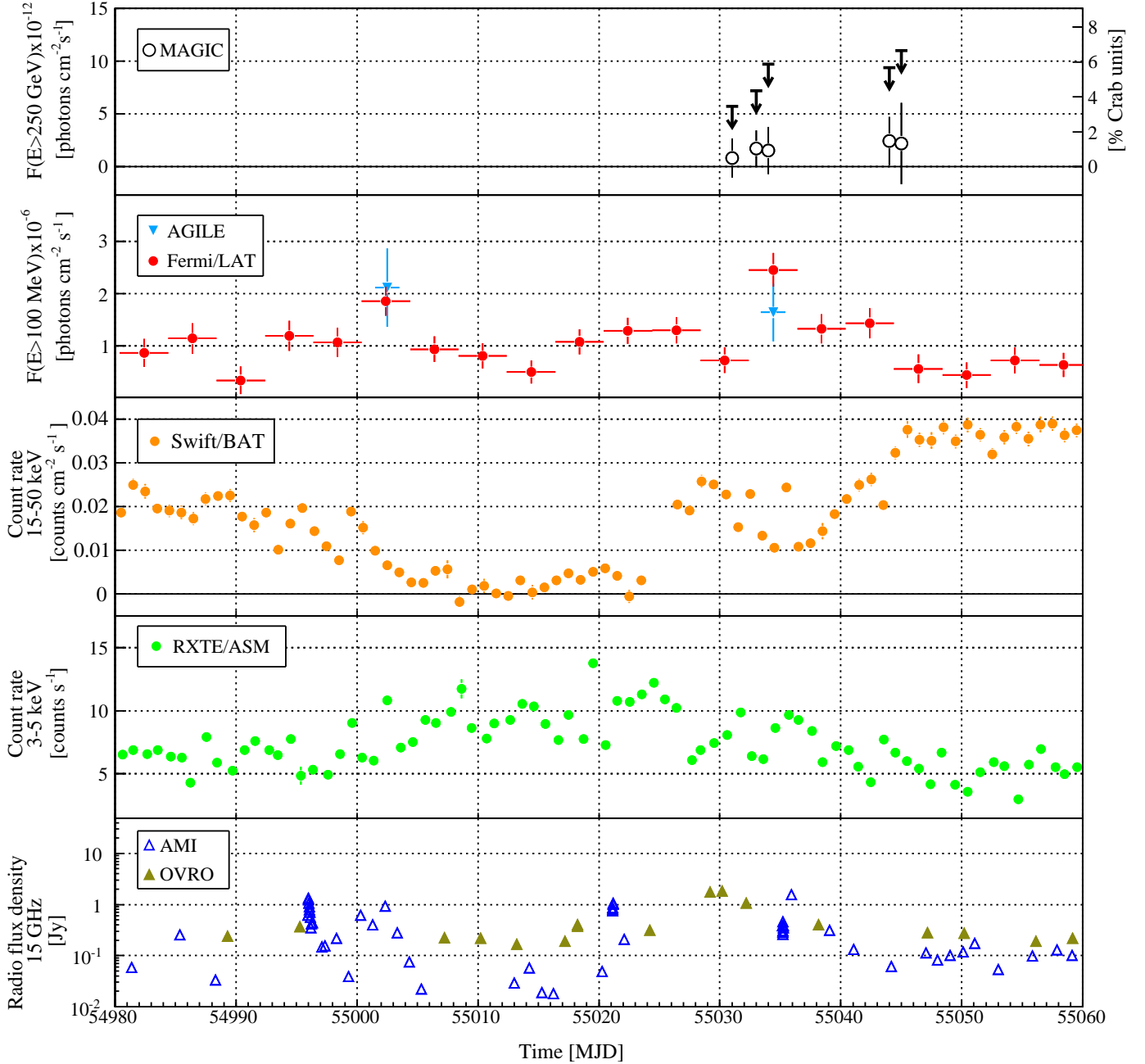


FIG. 3.— Zoom of Figure 2 around the cycle V campaign between 2009 May 29 and August 17. The open black points in the VHE MAGIC panel show the non-significant measured integral fluxes with their statistical error bars (whereas the ULs take into account also the systematic errors).

vational trigger. All the other observations were carried out when the source was in the SS. The first two MAGIC observational campaigns (cycles I and II) were triggered by flares at radio frequencies, which are expected when the source is in the SS. Unfortunately, the conditions on the trigger together with MAGIC constraints on observation time did not allow a simultaneous coverage of the flaring states: MAGIC started pointing toward Cygnus X-3 twelve and two days after the strong radio emission, respectively. On the other hand, in the last observational cycles (IV and V), MAGIC observed the source during the SS, following two *AGILE* alerts on a high-flux activity in the high-energy band: the GeV emission oc-

curs only in this X-ray spectral state. During the second alert, in 2009 July (MJD 55030), MAGIC recorded some data simultaneously with a GeV peak emission and did not detect any VHE signal. This important result will be discussed in detail in Section 4.1.

Microquasars are expected to produce VHE emission inside the jets either when they are compact and persistent, mainly in the HS, or in the presence of strong radio-emitting-blobs, which most likely happen during an SS. Therefore, the results of the MAGIC observations were divided according to the X-ray spectral state of the source, as described in Sections 4.2 and 4.3 for the SS and HS, respectively. Besides,



in the scenario where the VHE radiation is emitted during powerful synchrotron radio ejections, there might be a correlation between these two wavelengths (Atayan & Aharonian 1999). Therefore, in Section 4.4 the X-ray/radio states during the MAGIC observations are quoted.

#### 4.1. Results during High-energy $\gamma$ -ray Emission

Abdo et al. (2009) presented the *Fermi*/LAT observations of Cygnus X-3 between 2008 August 4 and 2009 September 2. They detected a strong signal above 100 MeV, with an overall significance of more than 29 standard deviations, which is mainly dominated by two active periods: MJD 54750–54820 and 54990–55045. These active periods coincide with the X-ray SS of the source, indicating that Cygnus X-3 emits high-energy  $\gamma$ -rays during this spectral state, with an average flux of  $1.2 \times 10^{-6}$  photons  $\text{cm}^{-2} \text{s}^{-1}$  and a photon index of  $2.70 \pm 0.05_{\text{stat}} \pm 0.20_{\text{sys}}$  (under the assumption of a power-law spectrum). They also estimated that the peak flux can be as high as  $2 \times 10^{-6}$  photons  $\text{cm}^{-2} \text{s}^{-1}$  without providing any photon index.

The five *AGILE* detections between 100 MeV and 3 GeV (Tavani et al. 2009; A. Bulgarelli et al., in preparation) coincide with the strongest high-energy outbursts, which can be seen overlapping them with the *Fermi*/LAT light curve. The *AGILE* integral flux averaged over the first four detections is estimated to be  $1.9 \times 10^{-6}$  photons  $\text{cm}^{-2} \text{s}^{-1}$  with a corresponding photon index of  $1.8 \pm 0.2$ .

In cycle V, MAGIC pointed at Cygnus X-3 during the second period of high-energy enhanced activity detected by *Fermi*/LAT, as shown in Figure 3. In particular, MAGIC carried out observations simultaneous with a GeV emission peak on 2009 July 21 and 22 (MJD 55033–55034), and it did not detect any VHE emission. The corresponding MAGIC integral flux ULs above 250 GeV are lower than 6% of the Crab Nebula flux.

Figure 4 shows the spectral energy distribution (SED) of Cygnus X-3 between 100 MeV and 5 TeV including MAGIC 95% CL upper limits at VHE, and the power-law spectrum in the high-energy range reported by both *AGILE* and *Fermi*/LAT. The spectra take into account the error on the photon index and the one on the integral flux, which is 30% and 40% for *Fermi*/LAT and *AGILE*, respectively. The SED for the average SS was obtained considering the average *Fermi*/LAT flux and MAGIC results of the SS data set. On the other hand, to obtain the SED during a high-energy emission peak, the MAGIC measurements simultaneous with the GeV emission peak and both *Fermi*/LAT and *AGILE* spectral power-law fits were used. The *Fermi*/LAT photon index during the peak was assumed to be the same as the one for the SS average flux. Being the latter dominated by the brightest phases of the  $\gamma$ -ray outburst, it can also be considered representative of the flaring activity. Both MAGIC ULs are consistent with the extrapolation of the *Fermi*/LAT spectra up to VHE, but not with the extrapolation of the harder *AGILE* spectrum, which would suggest a cutoff between some tens and 250 GeV.

#### 4.2. Results During the Soft State

The MAGIC telescope pointed at Cygnus X-3 when it was in the SS during the observational cycles I, II, IV and V, corresponding to a total of 30.8 hr. For these observations, soft X-ray measurements in the 3–5 keV band are always above the transitional level set at 3 counts  $\text{s}^{-1}$  by Szostek et al. (2008).

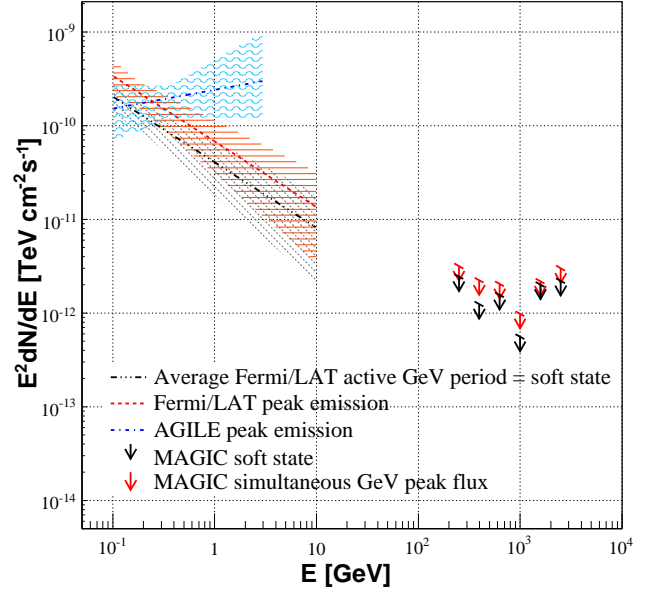


FIG. 4.— Cygnus X-3 SED in the high-energy and VHE bands. The lines indicate the power-law spectra derived from *Fermi*/LAT and *AGILE* integral fluxes and photon indices, where the corresponding errors were taken into account and are shown in shadowed areas. The arrows display the 95% CL MAGIC differential flux ULs and their slope indicates the assumed power-law spectrum with a photon index of 2.6. The black indicators show the SED during the period of enhanced GeV activity coinciding with the SS, whereas, the red and blue ones during the high-energy peak emission (MJD 55031–55034).

After having analyzed each data cycle separately, the data sets were combined in order to obtain a global UL to the integral flux for the SS. The UL at 95% CL for energies greater than 250 GeV is  $4.1 \times 10^{-12}$  photons  $\text{cm}^{-2} \text{s}^{-1}$ , i.e.,  $\sim 2.5\%$  of the Crab Nebula flux. The differential flux ULs for this spectral state are shown in Table 4 and in the left panel of Figure 5.

Due to the highly anisotropic radiation from the companion star, the predicted  $\gamma$ -ray emission above 250 GeV would be modulated according to the orbital phase (Bednarek 1997). Absorption might play an important role in making the VHE orbital modulation difficult to be detected by the current sensitivity instrumentation (Bednarek 2010). The orbital modulation of the GeV  $\gamma$ -ray emission was detected only when the source was in the SS (Abdo et al. 2009). MAGIC searched for such modulation in this spectral state. A phase-folded analysis was performed assuming the parabolic ephemeris in Singh et al. (2002). The results are shown in the left panel of Figure 6 and in Table 5. No evidence of VHE  $\gamma$ -ray signal was found in any phase bin. The obtained integral flux ULs are smaller than 10% of the Crab Nebula flux for all of them.

#### 4.3. Results During the Hard State

The 25.9 hr of MAGIC cycle III data sample were obtained when Cygnus X-3 was in the HS. *Swift*/BAT count rates during this cycle are rather high, greater than 0.05 counts  $\text{cm}^{-2} \text{s}^{-1}$ , whereas the soft X-ray fluxes in the 3–5 keV band are below 2 counts  $\text{s}^{-1}$ .

For this spectral state, the integral flux UL for energies greater than 250 GeV is 1.1% of the Crab Nebula flux ( $1.8 \times 10^{-12}$  photons  $\text{cm}^{-2} \text{s}^{-1}$ ). The differential flux ULs

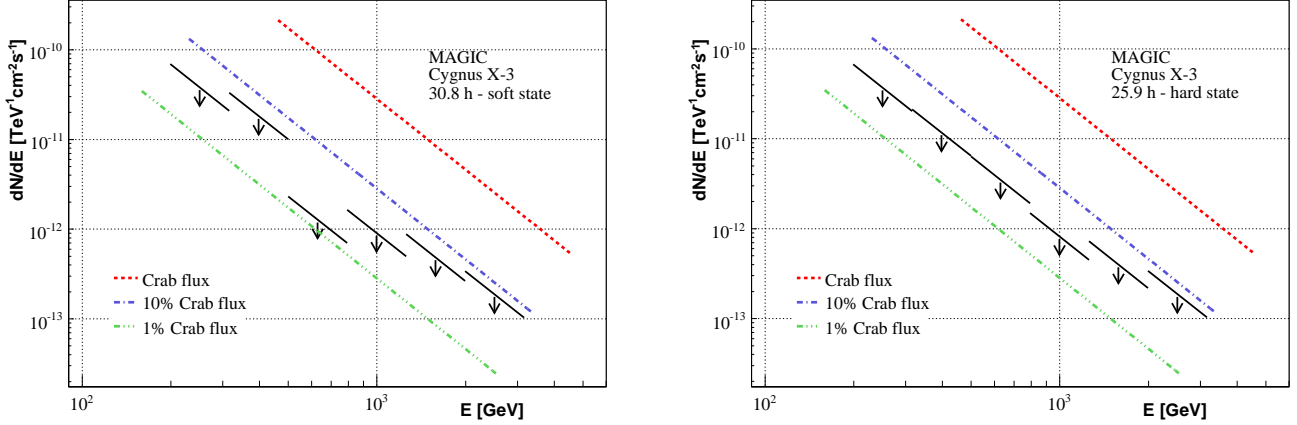


FIG. 5.— Ninety-five percent differential flux ULs for the SS (left panel) and HS (right panel) observations. The slope of the arrows indicates the assumed power-law spectrum with a photon index of 2.6.

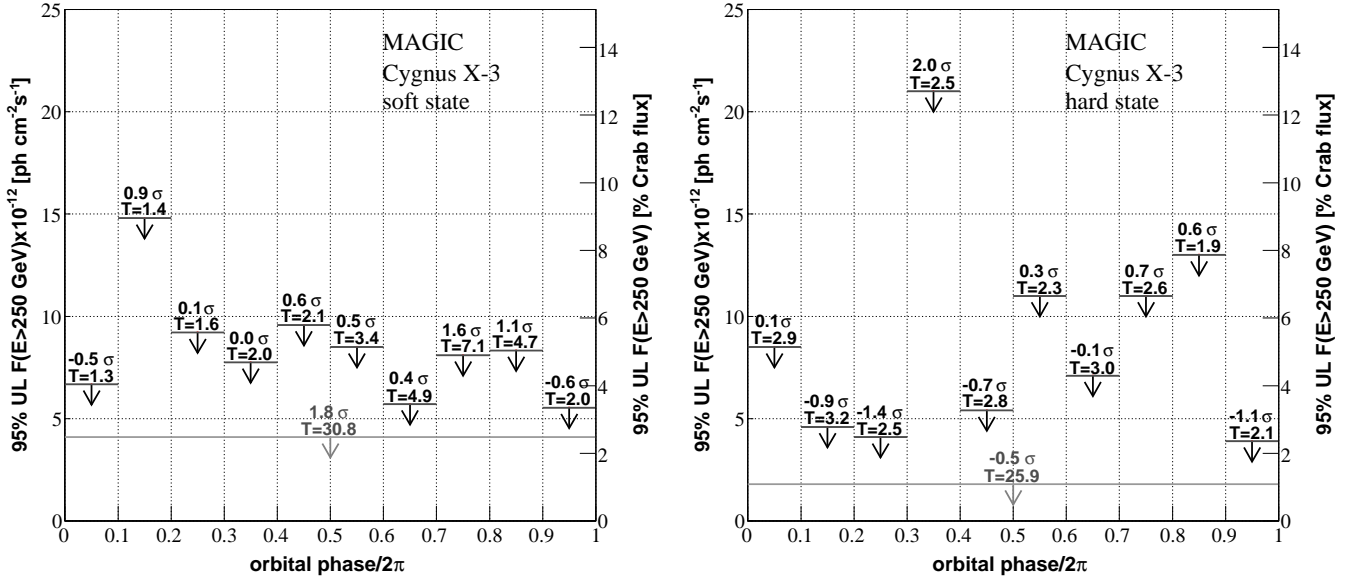


FIG. 6.— Phase-wise integral flux ULs for  $E > 250$  GeV for the SS (left panel) and HS (right panel). The effective observation time (in hours) and the signal significance for each phase bin are written on top of each arrow. The gray arrow indicates the integral flux UL on the VHE time-integrated emission.

are quoted in Table 4 and plotted in the right panel of Figure 5. The performed phase-folded analysis for this spectral state did not yield any significant detection. The computed ULs to the integral flux are, on average, at the level of 5% of the Crab Nebula flux (see the right panel of Figure 6 and Table 5).

#### 4.4. Results During X-ray/Radio Rates

MAGIC observed Cygnus X-3 in both X-ray main spectral states (see Sections 4.2 and 4.3). However, the state of the source can be further characterized by simultaneous radio flux. Szostek *et al.* (2008) identified six different X-ray/radio states studying simultaneous observations of the Green Bank Interferometer at 8.3 GHz and *RXTE*/ASM in the energy range 3–5 keV. The relation between these two energy bands is shown in the so-called saxophone plot (see Figure 7). It was

noted that the use of other radio frequencies yields similar results. This gives us the confidence that a direct comparison between their and our results using 15 GHz (RT and AMI) and 11.2 GHz (RATAN-600) is reasonable. The OVRO and AMI 15 GHz data generally agree well, but for an  $\sim 0.12$  Jy offset apparent during steady periods, probably due to unrelated extended emission resolved out by AMI. Thus, only the AMI 15 GHz were used in this analysis, although our conclusions are not substantially affected by this choice.

Figure 7 shows the soft X-ray (3–5 keV) *RXTE*/ASM count rates versus radio flux densities corresponding either to the nights of MAGIC observations for the five observational cycles or to the *AGILE* flux peaks (only the last four *AGILE* detections were considered since no simultaneous radio data were available for the first one). Unfortunately, no radio



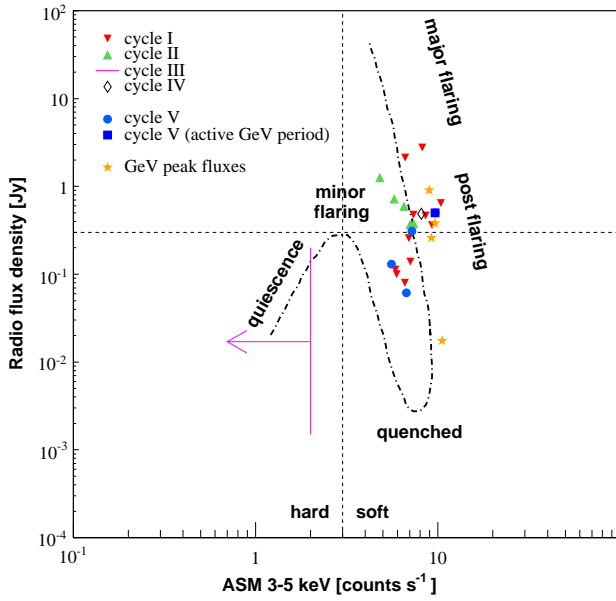


FIG. 7.— Soft X-ray counts vs. radio fluxes simultaneous with the GeV peak fluxes (yellow stars) and MAGIC observations, where the different marker colors identify the five MAGIC observational cycles. The pink arrow shows the X-ray flux level during the cycle III MAGIC campaign, for which radio data are not available. Radio measurements are at 11.2 GHz from RATAN-600 and at 15 GHz from RT/AMI. The dot-dashed line shows the expected “saxophone” shape, adapted from Szostek et al. (2008).

data simultaneous with cycle III and cycle IV MAGIC observations were available. Nevertheless, in the case of cycle III data, this does not prevent us from pointing out that Cygnus X-3 was in a quiescent state, just by using the soft X-ray measurements. For cycle IV data, quasi simultaneous radio observations (one day before MAGIC observations) were used. This latter choice does not affect our qualitative result since the source had already entered a post-flaring state. As shown in Figure 8, in 2008 April, *AGILE* detected Cygnus X-3 (MJD 54572–54573) one day before a major radio flare (Trushkin et al. 2008) lasting a few days, but MAGIC started pointing at the microquasar 10 days after the peak radio emission.

All the high-energy flux peaks were detected in the right branch of the “saxophone”, before, after, or during a flaring state. Although Abdo et al. (2009) quoted a time lag between the radio and the  $\gamma$ -ray peaks of  $5 \pm 7$  days, the correlation between the two energy bands is not yet clear. On the other hand, MAGIC observed Cygnus X-3 in its SS some days after the radio flare occurred (see Figures 8, 9), although for the first nights of cycle V observations, the radio flux densities are rather high and oscillating between two small flares (see Figure 3).

## 5. DISCUSSION

MAGIC observations of Cygnus X-3 cover all X-ray spectral states of the source in which VHE emission is thought to be likely produced either from a persistent jet in the HS or during powerful ejections in the SS. However, no significant excess events were found in any of the inspected samples.

VHE  $\gamma$  rays have been predicted from microquasar jets (Atoyan & Aharonian 1999; Romero et al. 2003;

Bosch-Ramon et al. 2006). A robust prediction of modeling is that photon–photon absorption cannot be neglected if the  $\gamma$  rays are produced close to a massive star (Bednarek 1997; Orellana et al. 2007). In particular for Cygnus X-3 the presence of a Wolf–Rayet companion, with temperature  $T_* \approx 10^5$  K and radius  $R_* \approx 10^{11}$  cm, leads to an optical depth  $\tau \geq 1$  for VHE  $\gamma$  rays for an emitter located at several orbital radii from the star (Bednarek 2010). Even under very efficient electromagnetic cascading, i.e., a radiation to magnetic energy density ratio  $8\pi u_*/B^2 \gg 1$ , the expected VHE fluxes are below the sensitivity of the present instruments (Bednarek 2010). Therefore, in order to detect VHE photons, the emitter should be located far from the binary system.

*Fermi*/LAT detected Cygnus X-3 when it was in the SS and found orbital modulation for the radiation above 100 MeV with a photon index of 2.7 for the periods of enhanced activity (Abdo et al. 2009). For the epochs outside these high-activity periods, the GeV flux decreases significantly (Figure 2 in Abdo et al. (2009)) and no modulation is found. The GeV orbital light curve of Cygnus X-3 in the high-energy active periods can be explained in the context of anisotropic inverse Compton scattering with the stellar photons (Abdo et al. 2009; Bosch-Ramon & Khangulyan 2009; Dubus et al. 2010), which is also energetically more efficient than hadronic mechanisms such as  $pp$  interactions or photomeson production. Since very bright X-ray emission is produced in the inner accretion disk or at the base of the jets in Cygnus X-3, the GeV radiation would be absorbed unless it is originated beyond  $\sim 10^{10}$  cm above the compact object. This implies that the GeV radiation is produced in the jet of Cygnus X-3 rather than in the inner accretion disk/corona region. On the other hand, the GeV emitter cannot be too high in the jet, since otherwise there would not be strong orbital modulation (see also Abdo et al. 2009). Therefore, the observed GeV and the predicted detectable VHE emission cannot be explained by one particular population because the former should be produced in/close to the system and the latter farther from it. The location of a hypothetical VHE emitter could coincide with the innermost region of the radio emitting jet, which, to avoid synchrotron self-absorption, should start relatively far from the binary system. This is consistent with the fact that MAGIC did not detect Cygnus X-3 during the high-activity GeV period, even though the flux ULs are close to a power-law extrapolation of the *Fermi*/LAT spectrum to energies greater than 100 GeV and well below an extrapolation of the *AGILE* spectrum.

During the periods of GeV high-activity of the source, as by the synchrotron self Compton scenario (Atoyan & Aharonian 1999), a detectable TeV signal could arise during the first hours of a radio outburst. Unfortunately, MAGIC has never observed the source during this phase of the flare, but always some days before or after the maximum radio flux. This radiation would not be strongly modulated, due to its origin far from the system. The two times more sensitive two telescopes arrangement, MAGIC phase II, may indeed detect Cygnus X-3 if it observes the source for longer time at the very maximum of a GeV flare, which might be even earlier than the onset of the radio outburst (Abdo et al. 2009).

In the HS, the VHE emission is expected to be produced inside the compact and persistent jets, whose total luminosity is estimated to be at least  $10^{37}$  erg s $^{-1}$  (Martí et al. 2005). The MAGIC VHE  $\gamma$ -ray UL set at  $1.1 \times 10^{-12}$  erg cm $^{-2}$  s $^{-1}$  is equivalent to a VHE luminosity of  $\simeq 7 \times 10^{33}$  erg s $^{-1}$

at 7 kpc. Thus, the maximum conversion efficiency of the jet power into VHE  $\gamma$  rays is 0.07% which is similar to that of Cygnus X-1 for the UL on the VHE steady emission, but 1 order of magnitude greater than that of GRS 1915+105 (Albert *et al.* 2007a; Acero *et al.* 2009). These ULs are in good agreement with the theoretical expectations which generally predict a VHE steady luminosity of  $\simeq 10^{32}$  erg s $^{-1}$ . Persistent galactic jets do not seem to be good candidate sources to be detected at VHEs by the current sensitivity instrumentation. Only 10 times more sensitive future instruments, such as Cherenkov Telescope Array, may have a chance to detect such VHE emission. This would provide a new handle on the emission mechanisms of compact jets.

## 6. ACKNOWLEDGMENTS

We thank the Instituto de Astrofísica de Canarias for the excellent working conditions at the Observatorio del Roque

de los Muchachos in La Palma. The support of the German BMBF and MPG, the Italian INFN, the Swiss National Fund SNF, and the Spanish MICINN is gratefully acknowledged. This work was also supported by the Polish MNiSzW Grant N N203 390834, by the YIP of the Helmholtz Gemeinschaft, and by grant DO02-353 of the Bulgarian National Science Fund. Sergei Trushkin is grateful for the support of the RATAN observations and the Russian Foundation for Basic Research, Grant N08-02-00504-a.

We credit the *Swift*/BAT and *RXTE*/ASM teams for making public their transient monitor and quick-look results, respectively. We also thank Stéphane Corbel for providing useful comments and information on the OVRO and *Fermi*/LAT light curves.

## REFERENCES

- Abdo, A. A., *et al.* 2009, *Science*, 326, 1512  
 Acero, F., *et al.* 2009, *A&A*, 508, 1135  
 Acciari, V. A., *et al.* 2008, *ApJ*, 679, 1427  
 Acciari, V. A., *et al.* 2009, *ApJ*, 700, 1034  
 Aharonian, F. A., *et al.* 2004, *ApJ*, 614, 897A  
 Aharonian, F. A., *et al.* 2005a, *A&A*, 442, 1  
 Aharonian, F. A., *et al.* 2005b, *Science*, 309, 746  
 Aharonian, F. A., *et al.* 2006, *A&A*, 460, 743  
 Albert, J., *et al.* 2006, *Science*, 312, 1771  
 Albert, J., *et al.* 2007a, *ApJ*, 665, L51  
 Albert, J., *et al.* 2007b, *arXiv:astro-ph/0702475*  
 Albert, J., *et al.* 2008a, *ApJ*, 675, L25  
 Albert, J., *et al.* 2008b, *ApJ*, 684, 1351  
 Albert, J., *et al.* 2008c, *ApJ*, 674, 1037  
 Albert, J., *et al.* 2008d, *Nucl. Instrum. Methods Phys. Res. A*, 594, 407  
 Albert, J., *et al.* 2008e, *Nucl. Instrum. Methods Phys. Res. A*, 588, 424  
 Albert, J., *et al.* 2009, *ApJ*, 693, 303  
 Aliu, E., *et al.* 2009, *Astropart. Phys.*, 30, 293  
 Anderhub H., *et al.* 2009, *ApJ*, 706, L27  
 Atoyan A. M., & Aharonian F. A. 1999, *MNRAS*, 302, 253  
 Becklin, E. E., Neugebauer, G., Hawkins, F. J., Mason, K. O., Sanford, P. W., Matthews, K., & Wynn-Williams, C. G. 1973, *Nature*, 245, 302  
 Bednarek W. 1997, *A&A*, 322, 523  
 Bednarek W. 2010, *MNRAS*, 406, 689  
 Bhat C. L., Sapru M. L., & Razdan H. 1986, *ApJ*, 306, 587  
 Bosch-Ramon, V., & Khangulyan, D. 2009, *Int. J. Mod. Phys. D*, 18, 347  
 Bosch-Ramon, V., Romero, G. E., & Paredes, J. M. 2006, *A&A*, 447, 263  
 Braes, L., & Miley, G. 1972, *Nature*, 237, 506  
 Breiman, L. 2001, *Mach. Learn.*, 45, 5  
 Britzger, D., Carmona, E., Majumdar, P., Blanch, O., Rico, J., Sitarek, J., & Wagner, R. 2009, in *Proc. 31st Int. Cosmic Ray Conf.*, *arXiv:0907.0973B*  
 Cawley M. F., *et al.* 1985, *ApJ*, 296, 185  
 Chadwick P. M., Dipper, N. A., Dowthwaite, J. C., Gibson, A. I., & Harrison, A. B. 1985, *Nature*, 318, 642  
 Chardin G., & Gerbier G. 1989, *A&A*, 210, 52  
 Danaher S., Fegan D. J., & Weekes T. C. 1981, *Nature*, 289, 568  
 Dowthwaite J. C. 1983, *A&A*, 126, 1  
 Dubus, G. 2006, *A&A*, 456, 801  
 Dubus, G., Cerutti, B., & Henri, G. 2010, *MNRAS*, 404, L55  
 Fomin, V. P., Stepanian, A. A., Lamb, R. C., Lewis, D. A., Punch, M., & Weekes, T. C. 1994, *Astropart. Phys.*, 2, 137  
 Geldzahler, B. J., *et al.* 1983, *ApJ*, 273, L65  
 Giacconi, R., Gorenstein, P., Gursky, H., & Waters, J. R. 1967, *ApJ*, 148, L119  
 Gregory, P. C., *et al.* 1972, *Nature (Phys. Sci.)*, 239, 114  
 Hanson, M. M., Still, M. D., & Fender, R. P. 2000, *ApJ*, 541, 308  
 Hillas, A. M. 1985, in *Proc. 19th Int. Cosmic Ray Conf.*, Vol. 3, ed. F. C. Jones, J. Adams, & G. M. Mason (Washington, DC: NASA), 445  
 Hjalmarsdotter L., Zdziarski, A. A., Paizis, A., Beckmann, V., & Vilhu, O. 2004, in *Proc. 5th Integral Workshop on the Integral Universe*, ed. V. Schönfelder, G. Lichti, & C. Winkler (ESA SP-552; Noordwijk:ESA), 223  
 Hjalmarsdotter L., Zdziarski, A. A., Larsson, S., Beckmann, V., McCollough, M., Hannikainen, D. C., & Vilhu, O. 2008, *MNRAS*, 384, 278  
 Koljonen K. I. I., Hannikainen, D. C., McCollough, M. L., Pooley, G. G., & Trushkin, S. A. 2010, *MNRAS*, 406, 307  
 Lamb, R. C., Godfrey, C. P., Wheaton, W. A., & Tumer, T. 1982, *Nature*, 296, 543  
 Levinson, A., & Blandford, R. 1996, *ApJ*, 456, L29  
 Ling, Z., Zhang, S. N., & Tang, S. 2009, *ApJ*, 695, 1111  
 Maraschi, L., & Treves, A. 1981, *MNRAS*, 194, 1  
 Martí, J., Paredes, J. M., & Peracaula, M. 2001, *A&A*, 375, 476  
 Martí, J., *et al.* 2005, *A&A*, 439, 279  
 Miller-Jones, J. C. A., Blundell, K. M., Rupen, M. P., Mioduszewski, A. J., Duffy, P., & Beasley, A. J. 2004, *ApJ*, 600, 368  
 Mioduszewski, A. J., Rupen, M. P., Hjellming, R. M., Pooley, G. G., & Waltman, E. B. 2001, *ApJ*, 553, 766  
 Mori, M., *et al.* 1997, *ApJ*, 476, 842  
 Orellana M., Bordas P., Bosch-Ramon, V., Romero, G. E., & Paredes, J. M. 2007, *A&A*, 476, 90  
 Parsignault, D. R., *et al.* 1972, *Nature*, 239, 123  
 Rico, J. 2008, *ApJ*, 683, L55  
 Rolke, W., Lopez, A., Conrad, J., & James, F. 2005, *Nucl. Instrum. Methods Phys. Res. A*, 551, 493  
 Romero, G. E., Torres, D. F., Kaufman Bernardo, M. M., & Mirabel, I. F. 2003, *A&A*, 410, L1  
 Sabatini, S., *et al.* 2010, *ApJ*, 712, L10  
 Saito, T. Y., *et al.* 2009, in *Proc. 31st Int. Cosmic Ray Conf.*, *arXiv:0907.1017S*  
 Samorski, M., & Stamm, W. 1983, *ApJ*, 268, L17  
 Schilling, M., Mang, O., & Siems, M. 2001, in *Proc. 27th Int. Cosmic Ray Conf.*, (Copernicus Gesellschaft) 2521  
 Singh, N. S., Naik, S., Paul, B., Agrawal, P. C., Rao, A. R., & Singh, K. Y. 2002, *A&A*, 392, 161  
 Stark M. J., & Saia M. 2003, *ApJ*, 587, L101  
 Szostek, A., Zdziarski, A. A., & McCollough, M. 2008, *MNRAS*, 388, 1001  
 Tavani, M., & Arons, J. 1997, *ApJ*, 477, 439  
 Tavani, M., *et al.* 2009, *Nature*, 462, 620  
 Trushkin, S. A., Nizhelskij, N. A., & Bursov, N. N. 2008, in *Proc. of the 2nd Kolkata Conference on Observational Evidence for Black Holes in the Universe*, AIP Conference Proc., 1053, 219  
 Tudose, V., *et al.* 2010, *MNRAS*, 401, 890  
 van Kerkwijk, M. H., *et al.* 1992, *Nature*, 355, 703  
 Vladimirovsky, B. M., Stepanian, A. A., & Fomin, V. P. 1973, in *Proc. 13th Int. Cosmic Ray Conf.*, ed. R.L. Chasson, 1, 456  
 Waltman, E. B., Fiedler, R. L., Johnston, K. L., & Ghigo, F. D. 1994, *ApJ*, 108, 179  
 Zdziarski A. A., & Gierlinski M. 2004, *Prog. Theor. Phys. Suppl.*, 155, 99

TABLE 2  
DIFFERENTIAL FLUX ULs FOR THE VHE TIME-INTEGRATED EMISSION AT 95% CL.

Energy Range (GeV)	$N_{\text{on}}$ Evt.s. <sup>a</sup>	$N_{\text{bg}}$ Evt.s. <sup>b</sup>	Excess Evt.s.	Norm.Fact. <sup>c</sup>	Signif. <sup>d</sup> ( $\sigma$ )	UL Evt.s. <sup>e</sup>	Flux UL ( $\text{TeV}^{-1}\text{cm}^{-2}\text{s}^{-1}$ )
199–315	4416	$4384.5 \pm 39.0$	$31.5 \pm 77.0$	0.34	0.4	237.8	$2.6\text{E}-11$
315–500	2057	$1980.6 \pm 28.6$	$76.4 \pm 53.6$	0.36	1.5	264.2	$1.2\text{E}-11$
500–792	769	$800.8 \pm 21.1$	$-31.8 \pm 34.9$	0.39	-0.9	51.3	$1.1\text{E}-12$
792–125	289	$299.9 \pm 12.9$	$-10.9 \pm 21.4$	0.38	-0.3	39.2	$5.1\text{E}-13$
1256–1991	102	$98.3 \pm 6.9$	$3.7 \pm 12.2$	0.37	0.5	36.2	$3.0\text{E}-13$
1991–3155	38	$32.3 \pm 3.5$	$5.7 \pm 7.1$	0.35	0.7	27.4	$1.3\text{E}-13$

<sup>a</sup> Number of signal events.

<sup>b</sup> Number of normalized background events.

<sup>c</sup> Normalization factor.

<sup>d</sup> Significance.

<sup>e</sup> Maximum number of excess events computed by using Rolke's method.

TABLE 3  
INTEGRAL FLUX ULs FOR ENERGIES ABOVE 250 GeV CALCULATED ON A DAILY BASIS AT 95% CL.

Date (MJD)	Time (h)	$N_{\text{on}}$ Evt.s.	$N_{\text{bg}}$ Evt.s.	Excess Evt.s.	Norm.Fact.	Signif. ( $\sigma$ )	UL Evt.s.	Flux UL ( $\text{cm}^{-2}\text{s}^{-1}$ )	(% C.U.)
53817	0.46	42	$41.4 \pm 1.8$	$0.6 \pm 6.7$	0.07	0.1	18.7	$1.2\text{E}-11$	7.5
53818	0.26	43	$27.0 \pm 0.7$	$16.0 \pm 6.6$	0.05	2.8	46.7	$5.7\text{E}-11$	34.2
53820	0.54	85	$83.8 \pm 4.6$	$1.2 \pm 10.2$	0.15	0.1	27.4	$1.5\text{E}-11$	9.3
53822	0.70	132	$111.4 \pm 3.5$	$20.6 \pm 12.0$	0.19	1.7	67.9	$2.9\text{E}-11$	17.4
53824	0.80	84	$84.8 \pm 2.4$	$-0.8 \pm 9.5$	0.15	-0.1	24.3	$9.1\text{E}-12$	5.5
53825	0.80	83	$64.3 \pm 2.1$	$18.7 \pm 9.3$	0.15	2.1	58.0	$2.2\text{E}-11$	13.1
53826	1.00	37	$34.3 \pm 0.6$	$2.7 \pm 6.1$	0.06	0.4	20.9	$6.1\text{E}-12$	3.7
53827	0.92	79	$76.5 \pm 1.9$	$2.5 \pm 9.1$	0.13	0.3	28.4	$9.1\text{E}-12$	5.5
53828	1.05	42	$49.3 \pm 1.1$	$-7.3 \pm 6.6$	0.09	-1.0	10.9	$3.1\text{E}-12$	1.8
53943	3.10	257	$274.3 \pm 9.5$	$-17.3 \pm 18.6$	0.33	-0.9	27.9	$4.1\text{E}-12$	2.5
53944	2.54	232	$235.7 \pm 8.8$	$-3.7 \pm 17.6$	0.33	-0.2	38.6	$7.1\text{E}-12$	4.3
53945	1.73	122	$125.7 \pm 6.4$	$-3.7 \pm 12.7$	0.33	-0.3	27.1	$8.4\text{E}-12$	5.1
53946	1.37	127	$108.0 \pm 5.9$	$19.0 \pm 12.7$	0.33	1.5	65.0	$2.5\text{E}-11$	15.3
53948	0.90	82	$65.7 \pm 4.6$	$16.3 \pm 10.2$	0.33	1.7	54.3	$3.2\text{E}-11$	19.4
53949	1.79	138	$143.3 \pm 6.9$	$5.3 \pm 13.6$	0.33	0.4	42.1	$1.3\text{E}-11$	7.8
54286	2.16	299	$314.0 \pm 10.2$	$-15.0 \pm 20.1$	0.33	-0.74	62.1	$1.1\text{E}-11$	6.8
54287	4.53	547	$547.0 \pm 13.4$	$-0.7 \pm 27.0$	0.33	-0.03	150.3	$1.3\text{E}-11$	8.1
54288	1.07	176	$208.0 \pm 8.3$	$-32.0 \pm 15.6$	0.33	-1.99	20.3	$7.0\text{E}-12$	4.3
54289	0.38	86	$84.3 \pm 5.3$	$1.7 \pm 10.7$	0.33	0.16	41.3	$3.9\text{E}-11$	23.5
54295	1.82	189	$176.3 \pm 7.6$	$12.7 \pm 15.7$	0.33	0.82	76.4	$2.1\text{E}-11$	13.0
54296	1.93	219	$209.0 \pm 8.3$	$10.0 \pm 17.0$	0.33	0.59	74.9	$2.0\text{E}-11$	11.8
54297	1.93	151	$138.7 \pm 6.7$	$12.3 \pm 14.0$	0.33	0.89	65.9	$1.7\text{E}-11$	10.4
54305	1.75	179	$167.7 \pm 7.4$	$11.3 \pm 15.3$	0.33	0.75	111.6	$3.1\text{E}-11$	19.0
54307	0.98	115	$117.0 \pm 6.2$	$-2.0 \pm 12.4$	0.33	-0.16	52.9	$2.4\text{E}-11$	14.5
54308	0.5	71	$59.3 \pm 4.4$	$11.7 \pm 9.5$	0.33	1.27	100.1	$8.1\text{E}-11$	48.8
54316	0.73	85	$88.7 \pm 5.4$	$-3.7 \pm 10.7$	0.33	-0.34	33.0	$1.8\text{E}-11$	11.0
54318	2.72	262	$277.3 \pm 9.6$	$-15.3 \pm 18.8$	0.33	-0.81	39.2	$6.7\text{E}-12$	4.1
54319	1.93	184	$184.0 \pm 7.8$	$0.0 \pm 15.6$	0.33	0.00	61.8	$1.5\text{E}-11$	8.8
54320	1.58	146	$152.3 \pm 7.1$	$-6.3 \pm 14.0$	0.33	-0.95	38.8	$1.1\text{E}-11$	6.8
54346	1.86	182	$200.0 \pm 8.1$	$-18.0 \pm 15.7$	0.33	-1.12	45.3	$1.0\text{E}-11$	6.3
54584	0.31	17	$23.0 \pm 2.7$	$-5.0 \pm 5.0$	0.33	-1.0	8.0	$1.0\text{E}-11$	6.2
54585	1.07	89	$75.3 \pm 5.0$	$13.7 \pm 10.7$	0.33	1.3	50.2	$2.0\text{E}-11$	11.9
54586	1.33	60	$66.7 \pm 4.7$	$-6.7 \pm 9.1$	0.33	-0.7	15.5	$5.1\text{E}-11$	3.1
55031	3.48	186	$183.3 \pm 7.8$	$2.7 \pm 15.7$	0.33	0.2	43.2	$5.7\text{E}-12$	3.4
55033	2.21	71	$63.7 \pm 4.6$	$7.3 \pm 9.6$	0.33	0.8	36.2	$7.2\text{E}-12$	4.4
55034	1.63	50	$43.3 \pm 3.8$	$6.7 \pm 8.0$	0.33	0.9	31.4	$9.7\text{E}-12$	5.8
55044	1.81	88	$80.0 \pm 5.1$	$8.0 \pm 10.7$	0.33	0.8	40.0	$9.4\text{E}-12$	5.7
55045	0.88	69	$69.0 \pm 4.8$	$0.0 \pm 9.6$	0.33	0.0	24.2	$1.1\text{E}-11$	6.6

NOTE. — Refer to Table 2 for the meaning of the columns.

TABLE 4  
DIFFERENTIAL FLUX ULs FOR THE SS AND HS OBSERVATIONS.

Spectral State	Energy Range (GeV)	$N_{on}$ Evt.	$N_{bg}$ Evt.	Excess Evt.	Norm.Fact.	Signif. ( $\sigma$ )	UL Evt.	Flux UL ( $\text{TeV}^{-1}\text{cm}^{-2}\text{s}^{-1}$ )
HS	199–315	1709	$1677.54 \pm 24.6$	$31.5 \pm 48.1$	0.36	0.7	169.2	$3.5\text{E}-11$
	315–500	926	$858.3 \pm 18.5$	$67.7 \pm 35.6$	0.40	1.9	212.3	$1.7\text{E}-11$
	500–792	324	$357.5 \pm 12.9$	$-33.5 \pm 22.2$	0.47	-1.1	30.3	$1.2\text{E}-12$
	792–1256	125	$124.9 \pm 7.7$	$0.1 \pm 13.6$	0.48	0.4	38.0	$8.4\text{E}-13$
	1256–1991	41	$33.7 \pm 3.9$	$7.3 \pm 7.5$	0.46	1.4	32.7	$4.5\text{E}-13$
	1991–3155	14	$8.7 \pm 1.8$	$5.3 \pm 4.2$	0.40	1.3	20.3	$1.7\text{E}-13$
LH	199–315	2707	$2707.0 \pm 29.9$	$0.0 \pm 60.0$	0.33	0.0	146.2	$3.4\text{E}-11$
	315–500	1131	$1122.3 \pm 19.2$	$8.7 \pm 38.7$	0.33	0.2	108.5	$1.1\text{E}-11$
	500–792	445	$443.3 \pm 12.1$	$1.7 \pm 24.3$	0.33	0.1	62.5	$3.3\text{E}-12$
	792–1256	164	$175.0 \pm 7.5$	$-11.0 \pm 14.9$	0.33	-0.7	24.7	$7.7\text{E}-13$
	1256–1991	61	$64.7 \pm 4.6$	$-3.7 \pm 9.1$	0.33	-0.4	18.4	$3.7\text{E}-13$
	1991–3155	24	$23.7 \pm 2.7$	$0.3 \pm 5.6$	0.33	0.1	15.2	$1.7\text{E}-13$

NOTE. — Refer to Table 2 for the meaning of the columns.

TABLE 5  
INTEGRAL FLUX ULs FOR ENERGIES ABOVE 250 GeV FOR THE PHASE-FOLDED ANALYSES OF THE OBSERVATIONS IN THE SS AND THE HS.

Spectral State	Phase	Time (h)	$N_{on}$ Evt.	$N_{bg}$ Evt.	Excess Evt.	Norm.Fact.	Signif. ( $\sigma$ )	UL Evt.	Flux UL ( $\text{cm}^{-2}\text{s}^{-1}$ )	(% C.U.)
SS	0.0–0.1	1.34	64	$68.0 \pm 4.7$	$-4.3 \pm 9.3$	0.33	-0.5	18.2	$6.7\text{E}-12$	4.0
	0.1–0.2	1.40	75	$67.3 \pm 4.7$	$8.3 \pm 9.8$	0.33	0.9	38.6	$1.5\text{E}-11$	8.9
	0.2–0.3	1.63	108	$107.0 \pm 5.9$	$1.3 \pm 12.0$	0.33	0.1	32.1	$9.2\text{E}-12$	5.6
	0.3–0.4	2.05	162	$162.0 \pm 7.3$	$0.3 \pm 14.6$	0.33	0.0	37.1	$7.7\text{E}-12$	4.7
	0.4–0.5	2.11	113	$106.0 \pm 5.9$	$7.3 \pm 12.1$	0.33	0.6	42.3	$9.6\text{E}-12$	5.8
	0.5–0.6	3.40	231	$222.3 \pm 8.5$	$8.7 \pm 17.5$	0.33	0.5	57.1	$8.5\text{E}-12$	5.1
	0.6–0.7	4.93	370	$361.3 \pm 10.2$	$9.1 \pm 21.8$	0.29	0.4	68.3	$5.7\text{E}-12$	3.4
	0.7–0.8	7.13	649	$600.7 \pm 17.1$	$49.4 \pm 30.7$	0.49	1.6	163.9	$8.1\text{E}-12$	4.9
	0.8–0.9	4.69	331	$310.0 \pm 8.4$	$21.2 \pm 20.0$	0.23	1.1	86.4	$8.3\text{E}-12$	5.1
	0.9–1.0	2.05	109	$116.0 \pm 6.2$	$-7.0 \pm 12.1$	0.33	-0.6	22.1	$5.5\text{E}-12$	3.3
	0–1	30.78	2216	$2120.3 \pm 29.5$	$96.3 \pm 55.5$	0.41	1.8	311.6	$4.1\text{E}-12$	2.5
HS	0.0–0.1	2.89	511	$509.7 \pm 12.9$	$1.3 \pm 26.1$	0.33	0.0	102.5	$8.6\text{E}-12$	5.2
	0.1–0.2	3.23	477	$501.3 \pm 12.8$	$-24.3 \pm 25.3$	0.33	-0.9	52.5	$4.6\text{E}-12$	2.7
	0.2–0.3	2.53	281	$308.0 \pm 10.1$	$-27.0 \pm 19.5$	0.33	-1.4	33.6	$4.1\text{E}-12$	2.5
	0.3–0.4	2.53	266	$230.0 \pm 8.7$	$36.0 \pm 18.5$	0.33	2.0	218.1	$2.1\text{E}-11$	12.4
	0.4–0.5	2.79	248	$261.0 \pm 9.2$	$-13.0 \pm 18.3$	0.33	-0.7	43.2	$5.4\text{E}-12$	3.3
	0.5–0.6	2.27	210	$205.3 \pm 8.2$	$4.7 \pm 16.6$	0.33	0.3	73.1	$1.1\text{E}-11$	6.8
	0.6–0.7	2.99	242	$243.0 \pm 8.9$	$-1.0 \pm 17.9$	0.33	-0.1	65.8	$7.1\text{E}-12$	4.3
	0.7–0.8	2.63	234	$222.7 \pm 8.6$	$11.3 \pm 17.5$	0.33	0.6	116.3	$1.1\text{E}-11$	6.8
	0.8–0.9	1.95	199	$189.7 \pm 7.9$	$9.3 \pm 16.2$	0.33	0.6	118.5	$1.3\text{E}-11$	7.8
	0.9–1.0	2.13	235	$261.3 \pm 9.3$	$-26.3 \pm 17.9$	0.33	-1.4	33.8	$3.9\text{E}-12$	2.4
	0–1	25.9	2903	$2932.0 \pm 31.1$	$-29.0 \pm 62.2$	0.33	-0.5	191.0	$1.8\text{E}-12$	1.1

NOTE. — Refer to Table 2 for the meaning of the columns.

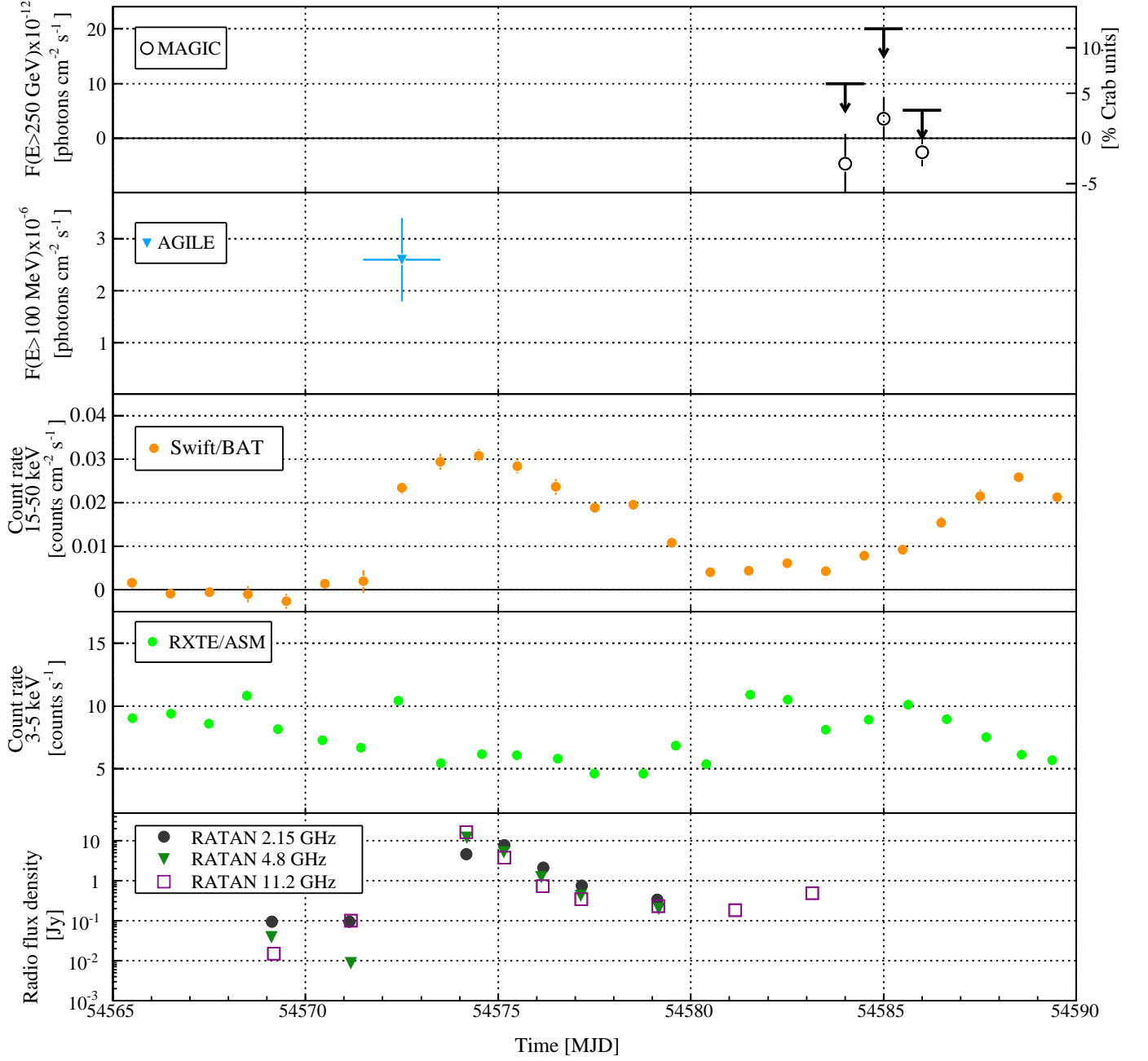


FIG. 8.— Zoom of Figure 2 around the cycle IV campaign between 2008 April 9 and May 2. The open black points in the VHE MAGIC panel show the non-significant measured integral fluxes with their statistical error bars (whereas the ULs take into account also the systematic errors).

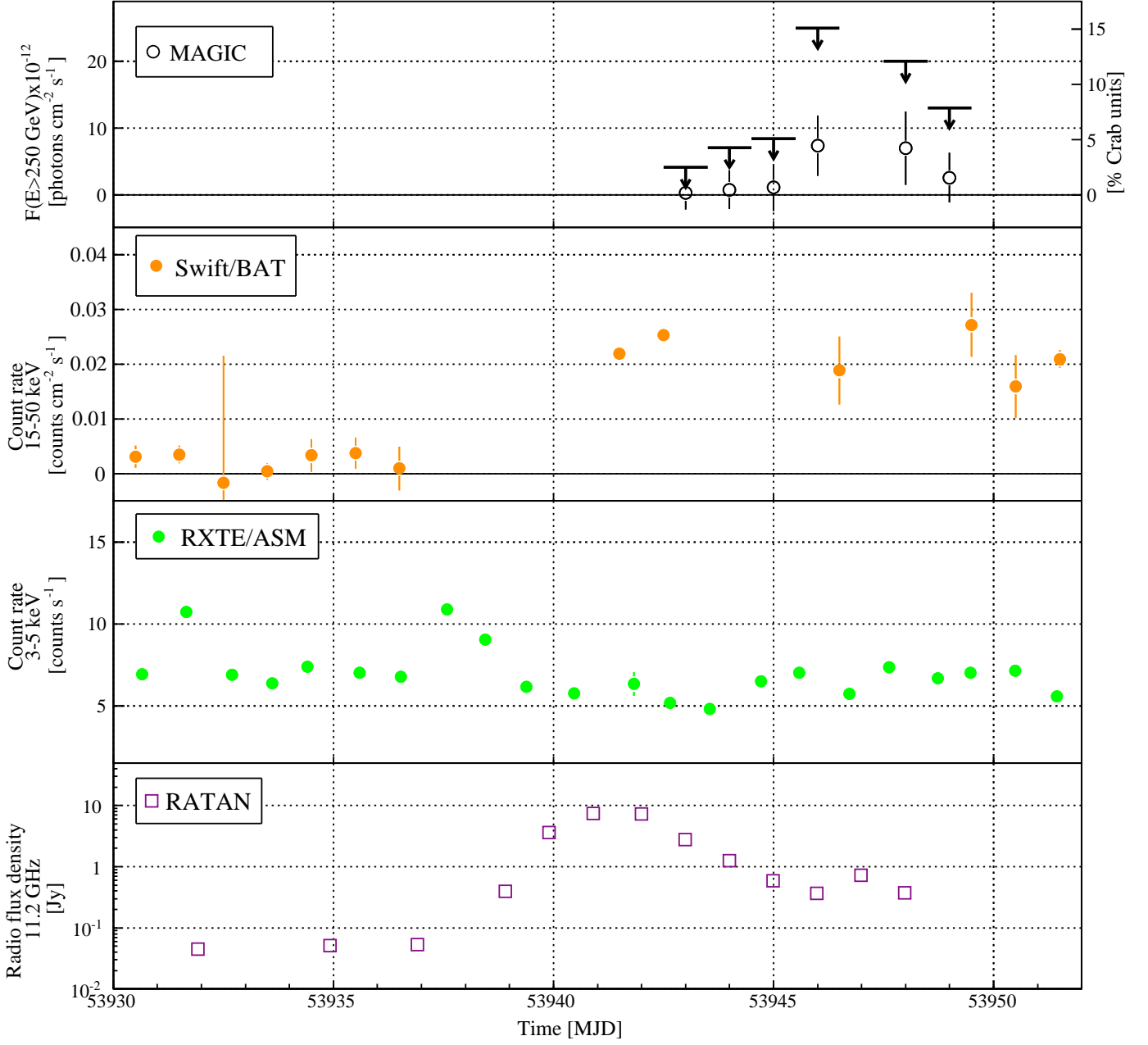


FIG. 9.— Zoom of Figure 2 around the cycle II campaign between 2006 July 14 and August 5. The open black points in the VHE MAGIC panel show the non-significant measured integral fluxes with their statistical error bars (whereas the ULs take into account also the systematic errors).